

## ARTICLE

## OPEN



# Photoinduced evolution of lattice orthorhombicity and conceivably enhanced ferromagnetism in $\text{LaMnO}_3$ membranes

Qinwen Lu , Yun Cheng <sup>3,8</sup>, Lijun Wu , Hongli Guo <sup>5,8</sup>, Fengfeng Qi <sup>3</sup>, Haijuan Zhang <sup>3</sup>, Junxiao Yu <sup>3</sup>, Qixin Liu <sup>1</sup>, Qing Wang <sup>2</sup>, Genhao Liang <sup>1,2</sup>, Jie Chen , Yalin Lu <sup>1</sup>, Jie Zhang , Dao Xiang , Jin Zhao , Yimei Zhu <sup>4</sup> and Xiaofang Zhai

Ultrashort laser pulses have been utilized to dynamically drive phase transitions in correlated quantum materials. Of particular interest is whether phases not achievable in thermal equilibrium can be induced in complex oxides with intricately coupled lattice, electron and spin degrees of freedom. Here, we tracked atomic motions in  $\text{LaMnO}_3$  following photoexcitation with MeV ultrafast electron diffraction (MeV-UED) technique. We found that the light excited state exhibits numerous signatures different from thermal equilibrium ones, including nearly conserved Bragg intensities, strongly suppressed La cation and oxygen anion displacements, and the long-range lattice orthorhombicity evolution. Furthermore, using first-principles calculations, we predict that the ferromagnetic ordering and conductivity are both enhanced upon laser excitation due to the reduction of the lattice orthorhombicity. This work benefits from recent advance in fabrication of membrane films with high epitaxial quality and in MeV-UED with large momentum space access and high temporal resolution.

*npj Quantum Materials* (2022) 7:47; <https://doi.org/10.1038/s41535-022-00456-4>

## INTRODUCTION

Strongly correlated quantum materials often possess rich phase diagrams due to the intricate coupling of multiple degrees of freedom and the delicate balance of competing orders, which offer an ideal platform for triggering many emergent physical phenomena. Conventionally, the tuning of material properties is achieved through classical methods, such as pressure, chemical doping, and epitaxial stress. Recently, there have been growing efforts in using light to manipulate and control the functionality of these fascinating materials<sup>1–4</sup>. Light-induced emergent phenomena, such as charge density waves<sup>5,6</sup>, superconductivity<sup>7–10</sup>, and hidden states<sup>11</sup>, to name a few, were reported in the past few years. Particular interest has been devoted to optically manipulating the correlated states of transition metal oxides with intriguing properties, including colossal magnetoresistance, ferroelectricity and high-temperature superconductivity<sup>12–20</sup>.

Capturing atomic motions following photoexcitation is essential for understanding the physics behind the optical control of macroscopic properties because an electronic structure is in many cases strongly coupled with its lattice. Recently, ultrafast X-ray diffraction (XRD) based on large scientific facilities such as synchrotrons and free electron lasers has achieved remarkable progress, making it possible to directly probe structural dynamics with extraordinary spatiotemporal resolution<sup>9,17,20</sup>. However, the momentum space detected by ultrafast XRD is relatively small and the accessibility to these large scientific facilities is rather limited. Alternatively, such structural dynamics may be studied with ultrafast electron diffraction (UED, see, for instance, refs. <sup>5,6,21–27</sup>), a table-top instrument complementary to ultrafast XRD and ultrafast spectroscopic techniques. In addition to the greatly reduced cost, the short de Broglie wavelength of electrons, especially at MeV

energies, also provides a large momentum space which particularly benefits the detection of high-index reflection peaks, crucial for accurate determination of atomic positions of transient events<sup>26–29</sup>. Furthermore, the orders-of-magnitude larger scattering cross-sections, compared with X-rays make electrons particularly suitable for probing small-volume samples such as thin films. Previously, UED has been used to observe the phase transition in  $\text{VO}_2$  and light-induced hidden states in  $\text{CeTe}_3$ ,  $\text{LaTe}_3$ , etc.<sup>5,6,22,23</sup>.

In MeV-UED experiments, a freestanding single-crystal sample with a thickness below 100 nm and a relatively large lateral size on the order of 100  $\mu\text{m}$  to match that of the electron beam is highly preferred. While layered materials with weak van der Waals forces can be cleaved to occasionally yield sufficiently large films, this scheme does not apply to most 3D transition metal oxides. Fortunately, a method using water-soluble sacrificial layers to prepare freestanding oxide membranes has recently been demonstrated<sup>30</sup>. With this technique, a substrate utilized in epitaxial growth can be removed to yield a freestanding membrane. For example, freestanding  $\text{BiFeO}_3$  and  $\text{BaTiO}_3$  ultrathin films have been successfully fabricated<sup>31</sup>, demonstrating attainability of single monolayer thickness for the former, and superelastic and even foldable for the latter<sup>32</sup>. Extreme tensile-strain states have also been reported in freestanding  $\text{La}_{0.7}\text{Ca}_{0.3}\text{MnO}_3$  membranes<sup>33</sup>. However, it is unclear whether such a membrane transferred to a hollow support has the required quality for UED experiments.

Here, we fabricated freestanding single-crystalline  $\text{LaMnO}_3$  thin films as large as  $10 \times 10 \text{ mm}^2$  and transferred them onto copper grids. The quality of the freestanding sample is sufficiently high that several hundreds of Bragg peaks and superlattice peaks are simultaneously observed, which is essential for accurate structural retrieval.  $\text{LaMnO}_3$  is chosen as the model system to illustrate the

<sup>1</sup>Department of Materials Science and Technology, Department of Physics, University of Science and Technology of China, 230026 Hefei, China. <sup>2</sup>School of Physical Science and Technology, ShanghaiTech University, Pudong, 201210 Shanghai, China. <sup>3</sup>Key Laboratory for Laser Plasmas (Ministry of Education), School of Physics and Astronomy, Collaborative Innovation Center of IFSA (CICIFSA), Shanghai Jiao Tong University, 200240 Shanghai, China. <sup>4</sup>Condensed Matter Physics and Materials Science Division, Brookhaven National Laboratory, Upton, NY 11973, USA. <sup>5</sup>Department of Physics and Astronomy, California State University Northridge, Northridge, CA 91330-8268, USA. <sup>6</sup>Tsung-Dao Lee Institute, Shanghai Jiao Tong University, 200240 Shanghai, China. <sup>7</sup>Zhangjiang Institute for Advanced Study, Shanghai Jiao Tong University, 200240 Shanghai, China. <sup>8</sup>These authors contributed equally: Qinwen Lu, Yun Cheng, Lijun Wu, Hongli Guo. email: dxiang@sjtu.edu.cn; zhaojin@ustc.edu.cn; zhu@bnl.gov; zhaixf@shanghaitech.edu.cn

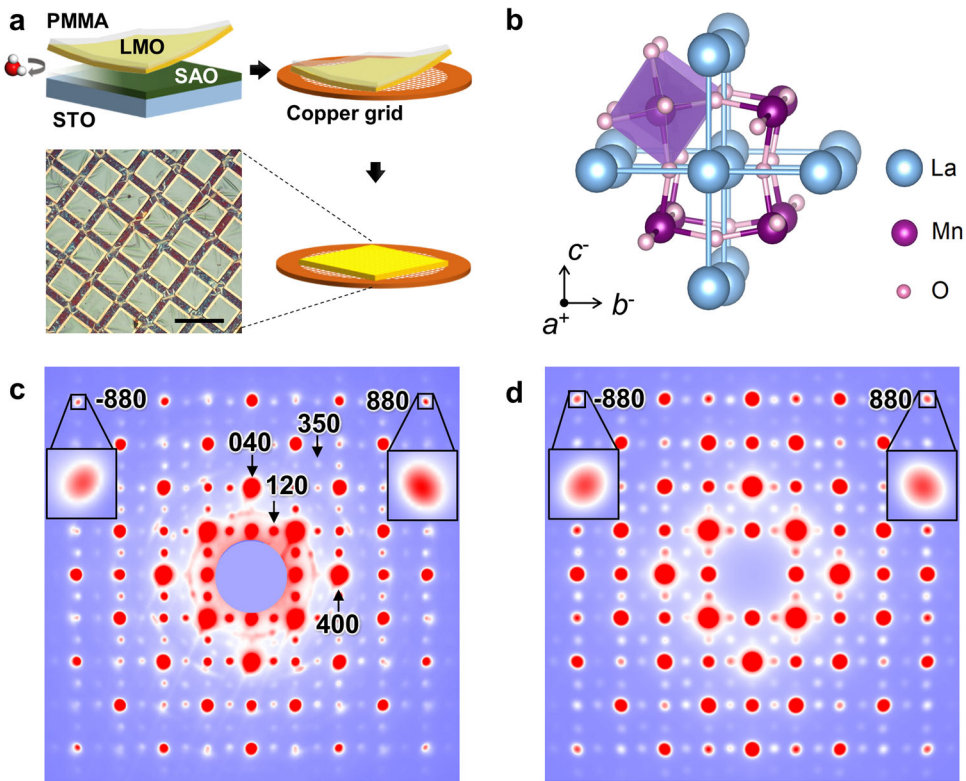


**Fig. 1 Freestanding LaMnO<sub>3</sub> film and its lattice dynamics measured by MeV-UED.** **a** Top: Schematic of the freestanding LMO film achieved by removing the SAO buffer layer grown on the STO substrate. Bottom: Optical microscopy image of the LMO film on the copper mesh grid for UED experiments. The scale bar is 100  $\mu\text{m}$ . **b** Schematic of orthorhombic structure of LaMnO<sub>3</sub>. **c** The experimental [001] UED pattern obtained before photoexcitation from the freestanding LaMnO<sub>3</sub> film. The transmitted beam was not included to avoid saturation of the detector. The bright spots marked as  $(h\ k\ 0)$  with  $(h, k)$  being (even, even), (odd, even), (even, odd), and (odd, odd) correspond to the Bragg reflections and superlattice reflections from the  $a^+b^-c^-$ ,  $a^-b^+c^-$ , and  $a^-b^-c^+$  twin variants, respectively. The  $(-880)$  and  $(880)$  spots are magnified showing their elliptical shape along the  $[110]^*$  and  $[-110]^*$  direction, respectively. **d** Simulated UED pattern based on the Bloch-wave method with the twin variants, showing good agreement with the experiment.

potential of UED in investigating the light-induced structural dynamics in the CMR manganites. Owing to the high temporal resolution of MeV-UED based on the double-bend achromat compressor<sup>28</sup> and its access to the large momentum space, the ultrafast lattice orthorhombicity change including the motion of atoms with different sub-lattice symmetries and the long-range lattice relaxation, is clearly visualized with high sensitivity and accuracy immediately after photoexcitation. We found that the light-induced transient phase exhibits a cubic-like structure with drastic reduction of lattice orthorhombicity signaled by reductions of La cation and oxygen anion displacements, together with suppressed long-range twinning. Using first-principles calculations we predict an excited transient state with enhanced ferromagnetic ordering accompanied by metallicity, which in practice leads to an enhanced high Curie temperature under light excitation. The detailed study reveals that the suppression of Jahn-Teller distortion being the result of repressed oxygen anion displacements, is the main driving force for the enhanced ferromagnetism and metallicity. Our work demonstrates the potential of UED in quantitatively understanding the light-induced dynamics in strongly correlated oxides that exhibit a large array of intriguing properties and order parameters, and paves the way for capturing more ‘hidden’ phases with functional properties in the CMR manganite oxides.

## RESULTS

### Fabrication of the freestanding LaMnO<sub>3</sub> membranes

The LaMnO<sub>3</sub> membranes, or films, are grown on water-soluble Sr<sub>3</sub>Al<sub>2</sub>O<sub>6</sub> buffer layers on insulating (001) SrTiO<sub>3</sub> substrates

using reflection high-energy electron diffraction (RHEED)-assisted pulsed laser deposition (PLD). Figure 1a shows the schematic fabrication process of the freestanding films (more details can be found in the “Methods” section). The optical microscope image in Fig. 1a illustrates a large and unbroken freestanding film on a hollow copper grid with an opening size of  $45 \times 45 \mu\text{m}^2$ . The XRD reciprocal space maps (RSMs) around the (103) and (013) Bragg peaks of the freestanding films are shown in Supplementary Fig. 1, demonstrating high single-crystalline quality of the films. Magnetization measurements show these films retain their ferromagnetic properties with  $T_c = 125$  K and a saturation magnetization of  $3 \mu_\text{B}$  per Mn (Supplementary Fig. 2). As shown in Fig. 1b, the bulk LaMnO<sub>3</sub> has an orthorhombic structure in the *Pbnm* space group and its oxygen octahedra exhibit an  $a^-b^-c^+$  rotation in the Glazer notation, where in-phase and out-of-phase rotation axes are indicated as ‘+’ and ‘-’ axes, respectively. In thin films, the  $a^+b^-c^-$  and  $a^-b^+c^-$  domains also known as  $a^+b^-c^-$  and  $a^-b^+c^-$  twin variants have been observed since the in-phase rotation axis (‘+’ axis) lies in the plane of the film<sup>34</sup>. Detailed atomic structures and their corresponding diffraction patterns are shown in Supplementary Figs. 3 and 4. In the reciprocal space of the orthorhombic structure, there are superlattice peaks related to oxygen octahedral rotations and La atom displacements<sup>35</sup>, which is essential for the transient atomic structure retrieval. One of the motivations to prepare high-quality freestanding films is to enable attaining distinct diffraction peaks that can infer subtle atomic motions upon photoexcitation.

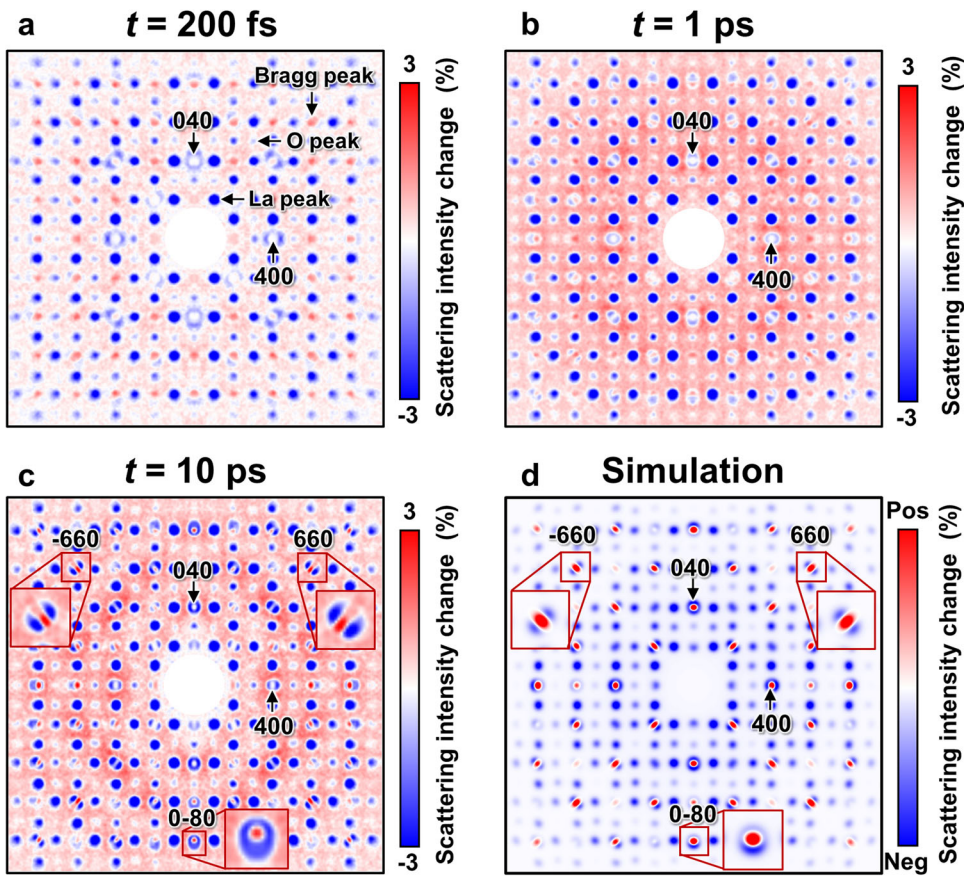


**Fig. 2 Evolution of the diffraction intensity at three key time delays.** **a–c** Experimental difference maps by subtracting the diffraction pattern before time zero from the diffraction pattern at  $t = 0.2$  ps (a),  $t = 1$  ps (b), and  $t = 10$  ps (c). **d** Simulated UED difference map of  $t = 10$  ps using the structure based on our observed lattice dynamics (see text). A few special reflections are magnified in (c) and (d) to show their distinctive intensity distributions in the difference map and the good agreement between experiments and calculations. Blue and red represent intensity decrease and increase, respectively. The pump fluence is  $6\text{ mJ cm}^{-2}$  for all UED measurements. In order to better display the results of  $\Delta\text{FWHM}$  transition, the color scale range is chosen to be  $\pm 3\%$  for which the intensity change higher than 3% is saturated.

### Structure revealed by the UED snapshots and simulations

The MeV-UED experiment is schematically shown in Supplementary Fig. 5. A representative  $(001)^*$  diffraction pattern of the  $\text{LaMnO}_3$  freestanding film measured with MeV electron beam is shown in Fig. 1c where the superlattice peaks are clearly seen. The observed  $(h\ 0\ 0)$  diffraction spots can be classified into three types. The first one is the brightest Bragg peaks with indices of (even, even, 0). The second is the much weaker superlattice peak of (odd, even, 0) and (even, odd, 0), mainly originated from the La displacements (shortened as La peaks, see Supplementary Fig. 6a, b) in the  $a^+b^-c^-$  and  $a^-b^+c^-$  domains, respectively. The third is the weakest peak (odd, odd, 0) that can be attributed to the oxygen octahedral tilt around the '+' axis or Jahn-Teller distortion in the  $a^-b^+c^+$  domain (see Supplementary Fig. 6k, l). An additional contribution to the (odd, odd, 0) peak intensity from the second order of La displacement in response to the oxygen octahedral rotation is also possible<sup>36,37</sup>. Nevertheless, the oxygen displacement is the main reason for the appearance of these peaks. We refer to these peaks as oxygen peaks.

A close inspection of Fig. 1c indicates the existence of symmetric, elliptical shaped diffraction spots, especially those along  $\langle 110 \rangle^*$  direction with high indices (for example the 880 and -880 spots shown in the insets of Fig. 1c). We attribute the elongation of these spots to twin variants, originated from the small difference in the  $a$  and  $b$  lattice parameters, which occur during film growth. The  $\text{MnO}_6$  octahedral in-phase rotation axis could lie along  $a$ ,  $b$  or  $c$  axis of the parent phase to form  $a^+b^-c^-$ ,

$a^-b^+c^-$  and  $a^-b^+c^+$  primary twin variants or domains. Here the parent phase is the pseudocubic substrate during film growth. For each primary twin variant, it can form four second twin variants by aligning their  $\{110\}$  plane with the  $\{110\}$  plane of the parent phase<sup>38</sup>. The UED pattern therefore is a superposition of 12  $\langle 001 \rangle$  zone diffraction patterns, each corresponding to an individual twin variant. When the lattice parameter along '+' axis and '-' axis are different, e.g.  $a \neq b$  in the  $a^+b^-c^-$  and  $a^-b^+c^-$  twin pair, the spots split because the '+' axis of the twin variant  $a^+b^-c^-$  rotated about 90° with respect to the  $a^-b^+c^-$ , as shown in Supplementary Fig. 7g. Note, we define the in-phase rotation axis ('+' axis) as the  $a$ -axis for all twin variants in Supplementary Fig. 7 to describe the twining relationship that is commonly used in crystallography. Under such a notation, because all twin variants have the same lattice in which the '+' axis is assigned to the  $a$ -axis, the  $[001]$  or  $[010]$  of the  $a^+b^-c^-$  and  $a^-b^+c^-$ , and the  $[100]$  of the  $a^-b^-c^-$  domains are parallel to the film normal. For simplicity in Figs. 1 and 2 we index the diffraction patterns based on a universal description of lattice of the twin variant  $a^+b^-c^-$ , as circled in Supplementary Fig. 7a. Because of the relatively large size of the electron beam, the spots we observed are significantly broadened and the spot split becomes elongation (Supplementary Fig. 7h). In the simulations, we reached excellent agreement between the simulated UED pattern (Fig. 1d) and the experiment (Fig. 1c) based on the 12 twin variants in the system, when using the lattice parameter of 7.876 Å for the '-' axes and 7.772 Å for the '+' axis with octahedral rotation angles of 7.5° and 6.0° for the '-' rotation and '+' rotation, respectively. In the simulation, the Jahn-Teller

distortion is taken to be  $Q_2 = 0.19 \text{ \AA}$  and  $Q_3 = 0.13 \text{ \AA}$ , and the corresponding La displacement is  $d = 0.01 \text{ \AA}$ . The diffraction patterns were convoluted with a point spread function to take into account the effect of the electron beam size.

### Time-resolved diffraction measurements

A 30 fs laser with a center wavelength of 800 nm is used as the pump pulse for photoexcitation, and the relativistic electron beam with  $\sim 3$  MeV kinetic energy is used as the probe pulse to record the atomic motion<sup>28</sup>. The UED measurements are performed at 300 K and the detected changes of the diffraction intensity ( $\Delta I(t)$ ) with respect to those before photoexcitation as a function of time are illustrated in movies (see the Supplementary Videos 1 and 2). The image change depicts the diffraction difference between the initial  $t = 0$  and the time  $t$ , which is termed the transient change. Figure 2 shows the transient changes in the diffraction intensity at three representative time delays. As shown in Fig. 2a, at the time delay of 200 fs the transient intensities of the La and oxygen peaks decrease with the intensity of the La peaks dropping faster than those of the oxygen peaks. The Bragg peaks show very interesting features. The intensity of the central part of the Bragg peaks increases after photoexcitation, while their surround and shoulder decrease for  $h00/0k0$  and  $hh0/h-h0$  spots, respectively. These features become more obvious with the increase of the time delay. As shown in Fig. 2c ( $t = 10$  ps), the spot shape of  $-080$  show a 'bean'-like feature, while those of  $880/660$  and  $-880/-660$  show 'butterfly'-like (insets in Fig. 2c) feature. Note, the direction of the 'butterfly' rotates 90° from  $880/660$  to  $-880/-660$ . These features are related to the evolution of the spots shape, more accurately the change of the distance between the two superimposed twining related spots, during photoexcitation. The elliptical spots, e.g.  $-880$  and  $880$ , become circled spots, while the circled spots, e.g.  $-800$  and  $080$ , becomes smaller after photoexcitation.

The spots shape change can be clearly seen in the quantitative measurements of the full width at half maximum (FWHM) of the diffraction peaks as a function of time delay for the spots  $-880$  and  $880$  (Fig. 3a, b) as well as  $-800$  and  $080$  (Supplementary Fig. 8) along both  $[-110]^*$  and  $[110]^*$  direction. Because of twining, each spot shown in Fig. 2 represents a superposition of several splitted spots (Supplementary Fig. 7). The change of spots shape is due to the change of the distances between these spots, which can be attributed to the change of the orthorhombicity in the structure. As shown in Supplementary Fig. 7, the relatively large lattice constant difference between in-phase '+' and out-of-phase '-' axes (7.772 Å for '+' axis and 7.876 Å for '-' axes) in the  $a^+b^-c^-$  and  $a^-b^+c^-$  twin variants results in large spot splitting (Supplementary Fig. 7g), thus increased spots size for  $(800)$  and  $(080)$  and elliptical shape for  $(-880)$  and  $(880)$  when the split spots are convoluted with the instrument point-spread-function (Supplementary Fig. 7h). With the reduction of the orthorhombicity due to suppressed octahedral tilt, Jahn-Teller distortion and La displacement, e.g. the reduced lattice constant difference between '+' and '-' axes (7.825 Å for '+' axis and 7.845 Å for '-' axes), the spots splitting decreases (Supplementary Fig. 7i), resulting in the decrease of the spots size  $(800)$  and  $(080)$  as well as the ellipticity  $(-880)$  and  $(880)$  (Supplementary Fig. 7j). When we subtract the pattern in Supplementary Fig. 7j from that in Supplementary Fig. 7h, we obtain the calculated difference map, as shown in Fig. 2d, which agrees with the experimental UED very well, confirming the reduction of the orthorhombicity after photoexcitation. Furthermore, this elucidation is cross checked by the  $\mathbf{Q}$  vector change of La peaks as shown in Fig. 3c, d. The  $\mathbf{Q}$  value of the  $(-1 -2 0)$  La peak, from the  $a^+b^-c^-$  domain, decreases along the  $[100]^*$  direction while increases along the  $[010]^*$  direction. It indicates the lattice expansion along the  $a^+$  axis with its originally small lattice constant, and compression along the  $b^-$  axis with its originally large lattice constant. As a result,

the in-plane lattice becomes more square-like. Similarly, the  $\mathbf{Q}$  value change of the  $(2 -1 0)$  peak from the  $a^-b^+c^-$  domain demonstrates the same trend of a more squared lattice change. Note the  $\mathbf{Q}$  values of La peaks change on a similar timescale as the FWHM changes of Bragg peaks. We therefore conclude that the change of both Bragg peak shape and La peak position agrees with the reduction of lattice orthorhombicity in the time period from 0 to 10 ps.

To reveal the detailed time dependence of the structure transition that leads to diffraction changes in Fig. 2, we further analyze the integrated diffraction intensities of the oxygen peak, the La peak and the Bragg peak as a function of time delay. Figure 3e, f shows the transient intensity changes of the La peak, the oxygen peak, and the Bragg peak. In the small time window (0–2 ps) shown in Fig. 3e, it can be seen that the oxygen and La peak intensities both decrease with time, being consistent with a gradual evolution from the orthorhombic to the cubic structure. To quantify the timescale of the diffraction dynamics, we fit the normalized intensity using following Eq. (1) to account for a fast-process and a slow process<sup>39</sup>.

$$I = I_0 + A_1 e^{-(t-t_0)/\tau_1} + A_2 e^{-(t-t_0)/\tau_2} \quad (1)$$

where  $A_1/\tau_1$  and  $A_2/\tau_2$  are the amplitude and decay times of the fast and slow components, respectively. The fitted lines are shown in Fig. 3e and f. We found that the oxygen peak only has a fast decay process with  $\tau_1 = 220 (\pm 26)$  fs, while the La peak has both a fast and a slow decay process with  $\tau_1 = 140 (\pm 24)$  fs (in Fig. 3e) and  $\tau_2 = 1.70 (\pm 0.37)$  ps (in Fig. 3e, f), respectively. Since the La displacement originates from the local charge-imbalance caused by the orthorhombic type oxygen-octahedron-rotation, it is reasonable that the La and oxygen peaks share similar dynamic behavior<sup>35</sup>. It should be noted that the slow process is not observed for the oxygen peaks, indicating that the reduction of the in-phase oxygen octahedral tilt around the '+' axis and Jahn-Teller distortion mainly happens in the fast process because the oxygen peaks are predominantly caused by the in-phase tilt and Jahn-Teller distortion (Supplementary Fig. 6k, l). Although we are unable to measure the out-of-phase ('-' rotation) octahedral tilt because its contribution to superlattice peaks is negligible in the  $\langle 001 \rangle$  zone UED pattern (Supplementary Fig. 6b, f, j), we anticipate that the out-of-phase tilt decreases until 10 ps in accordance with the reduction of the observed La displacement and lattice orthorhombicity in the slow process. In contrast, the Bragg peak intensities first increase and then decrease. The initial increase can be explained by the symmetry enhancement after optical excitation, similar to that observed in charge density wave materials when the periodic lattice distortion is reduced<sup>21</sup>, and the subsequent decrease is due to the increased temperature of the lattice, known as the Debye-Waller effect. Moreover, as shown in Supplementary Fig. 9a, a noticeable intensity oscillation near 2.5 THz is observed for the La peak. Such an oscillation mode has been assigned to the A-site atom vibration<sup>40–42</sup>.

### First-principles calculations

The UED measurements show a clear difference between the initial orthorhombic structure and the transient near-cubic structure after photoexcitation. The main changes include the significantly suppressed La and oxygen displacements, as well as the lattice orthorhombicity. Because the change of the oxygen atom position, also known as the Mn–O–Mn bond angle, is very important in tuning the double exchange and super exchange interaction of the CMR manganite oxide<sup>34,43</sup>, it is interesting to explore whether the photoexcitation also alters magnetic behavior in the transient state.

By performing first principles calculations (details can be found in the "Methods" section), we show that the photo-induced structural changes lead to the enhancement of both

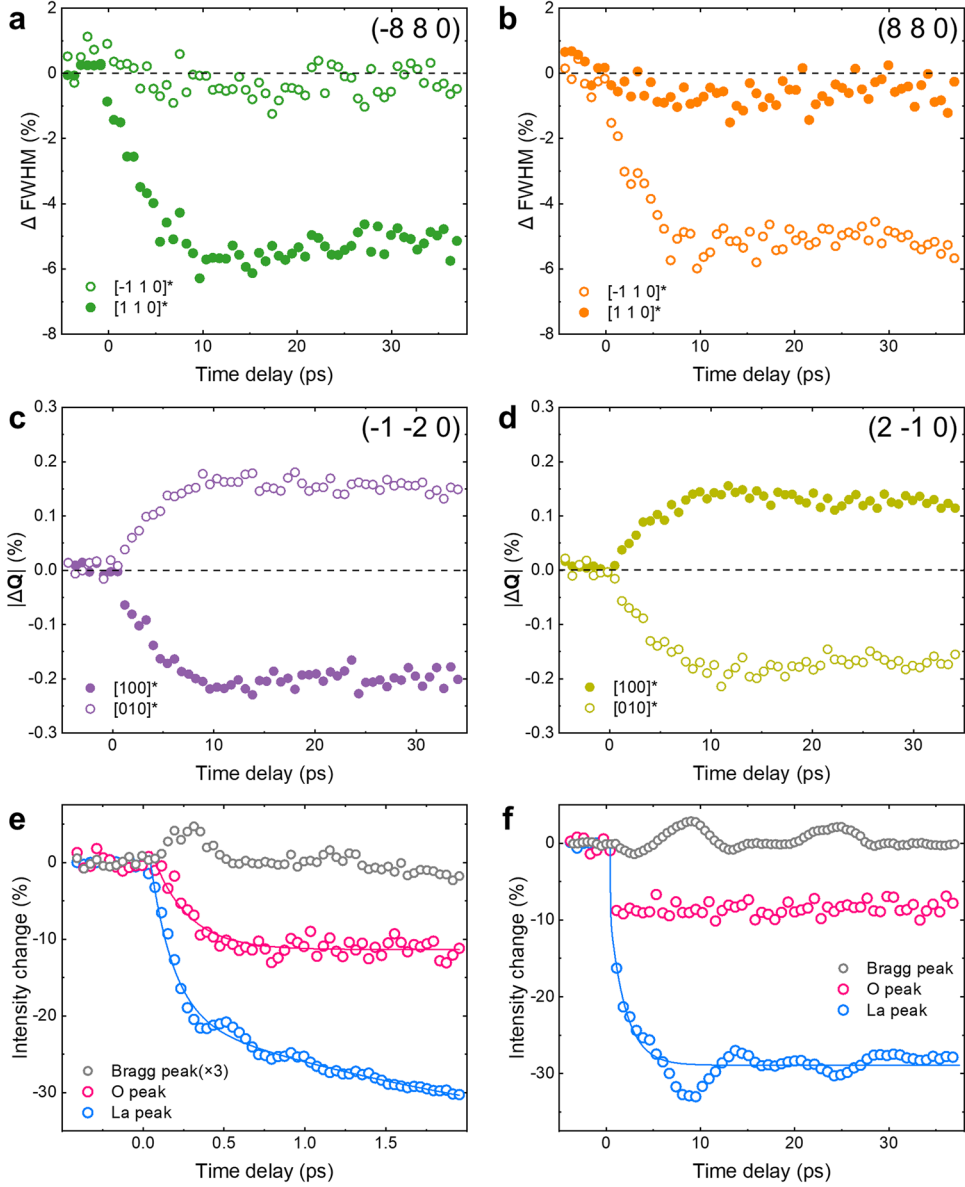


**Fig. 3** Diffraction peak widths (FWHM) and intensity as a function of time delay. **a, b** The change of FWHM of the  $(-880)$  and  $(880)$  Bragg peaks measured along the  $[110]^*$  and  $[-110]^*$  directions. **c, d** The change of  $|\Delta Q|$  along the  $[100]^*$  and  $[010]^*$  directions for  $(-1-20)$  (**c**) and  $(2-10)$  (**d**). **e** Bragg peaks (gray circles) and superlattice peaks induced by the  $MnO_6$  octahedral tilt/Jahn-Teller distortion (pink, O peak) and La displacements (blue, La peak). **f** Intensity evolution of the Bragg peaks, O peaks and La peaks on a long timescale. The indices in (**e**) and (**f**) are  $(6\ 6\ 0)$ ,  $(1\ 2\ 0)$ , and  $(3\ 5\ 0)$  for the Bragg peak, La peak and oxygen peak, respectively. (**e**) and (**f**) solid lines represent the exponential fits discussed in the main text.

ferromagnetism and metallicity. Figure 4a shows the optimized structure (labeled as Struct 1) using lattice constant obtained from the UED simulation ( $7.876\ \text{\AA}$  for the two '−' rotation axes and  $7.772\ \text{\AA}$  for the '+' rotation axis). The rotation angles are  $7.5^\circ$  for the '−' axes and  $6.0^\circ$  for the '+' axis, similar to those used in the simulation at  $t = 0\ \text{ps}$ . We further model three structures that represent three characteristic cells with reduced orthorhombicity. The rotation angles and Jahn-Teller distortion ( $Q_2$ ,  $Q_3$ ) are summarized in Table 1.  $Q_2$  and  $Q_3$  represent the in-plane and out-of-plane Mn-O bond breathing distortion, respectively (see Supplementary Fig. 10). For Struct 2, the rotation angle decreases but Jahn-Teller distortion remains the same as Struct 1. For Struct 3, the rotation angle further decreases and Jahn-Teller distortion is strongly decreased, which has the same rotation angles and lattice constants as those at  $t = 10\ \text{ps}$  in the simulation ( $2^\circ$  along three directions,  $7.845\ \text{\AA}$  along the two '−' rotation axes and

$7.825\ \text{\AA}$  along the '+' rotation axis). At last, we simulate a structure without rotation ( $a^0b^0c^0$ ) and Jahn-Teller distortion (Struct 4). Figure 4b shows the changes of magnetic exchange constants from Struct 1 to Struct 4. We use  $J_c = \frac{1}{32}(E_{\text{A-AM}} - E_{\text{FM}})$  to represent the interplane magnetic coupling, where  $E_{\text{A-AM}}$  is the energy of A-type antiferromagnetic phase and  $E_{\text{FM}}$  is the energy of ferromagnetic phase.  $J_{ab} = \frac{1}{64}(E_{\text{G-AM}} - E_{\text{A-AM}})$  represents the intraplane magnetic coupling, where  $E_{\text{G-AM}}$  the energy of G-type antiferromagnetic phase<sup>44</sup>. Both  $J_c$  and  $J_{ab}$  are positive and increasing when the structure changes from 1 to 4. However,  $J_{ab}$  and  $J_c$  only increase slightly as the structure transits from Struct 1 to Struct 2 in which only octahedral rotation occurs. On the other hand, when both the octahedral rotation and the Jahn-Teller distortion are suppressed from Struct 2 to Struct 3 and to Struct 4,  $J_{ab}$  and  $J_c$  increase more dramatically. Both the decreased rotation and the suppressed Jahn-Teller distortion are known to enhance

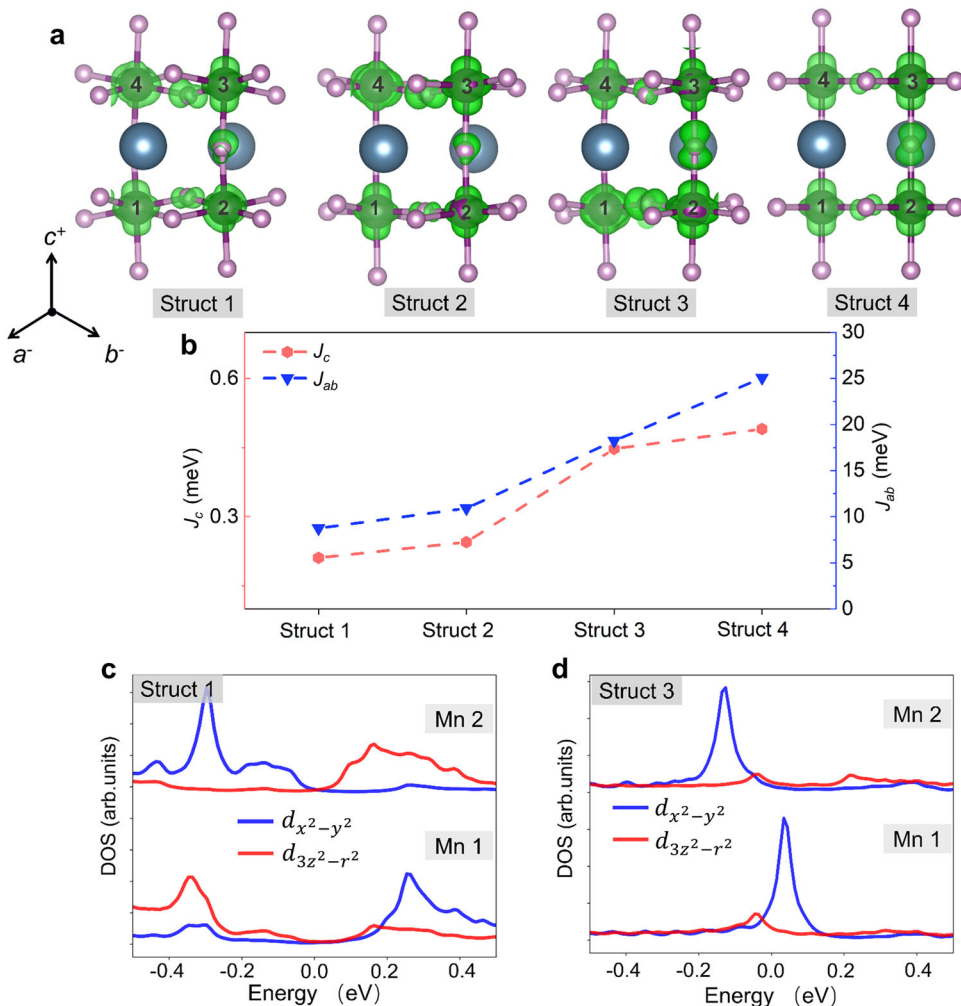


**Fig. 4 The enhancement of ferromagnetism and metallicity by photo-induced structural changes.** **a** The atomic structures (Struct 1–4) used in first-principles calculations and their corresponding charge density distributions of orbitals near Fermi level. **b** The changes of magnetic exchange constants for the four structures used in the calculations. (Struct. 1–Struct. 4). **c, d** the projected Density of States (DOS) for  $e_g$  orbitals of the major spin of the two nearest Mn atoms (labeled as Mn 1 and Mn 2) in Struct 1 (**c**) and Struct 3 (**d**). Blue lines are projected DOS of  $d_{x^2-y^2}$  orbital, red lines are projected DOS of  $d_{3z^2-r^2}$  orbital.

the ferromagnetic interaction<sup>44</sup>. The current calculation indicates that suppression of the Jahn–Teller distortion may have a strong influence on boosting ferromagnetism.

Furthermore, the ground state of the film turns from the insulating state with a 0.14 eV indirect gap in Struct. 1 to the ferromagnetic metallic state in Struct. 2–4 as shown by the band structures in Supplementary Fig. 11a–d. Specifically, we find that the energy of conduction band edge at  $\Gamma$  point crosses the fermi level in Struct 2. Furthermore, the direct gap at Y, M and X points significantly reduces in Struct 3 and finally closes at M point in Struct 4. For the ferromagnetic insulating phase of Struct 1, the G-type  $d_{3z^2-r^2}/d_{x^2-y^2}$  orbital order is observed as shown by the charge density distributions of orbitals near Fermi level (first panel in Fig. 4a) as well as the projected density of states (DOS) of the two nearest Mn atoms (labeled as Mn 1 and Mn 2) in Fig. 4c. It can be seen that the conduction/valence band edge is dominated by Mn 3d  $e_g$  orbitals with majority spin. In Struct 1, Mn 1(2) is equivalent to Mn 3(4) due to the symmetry of the G-type checkboard order. For Mn 1 atoms, the charge density is mostly originated from  $d_{3z^2-r^2}$  orbitals, and for Mn 2 atom, charge density is dominantly contributed by  $d_{x^2-y^2}$  orbitals. Compared to the FM insulating phase in Struct 1, the orbital order in FM metallic states is suppressed in Struct 2 and 3 and completely vanishes in

Struct 4. The equivalency between Mn 1(2) and Mn 3(4) is broken in Struct 2 and 3, and more mixed and combined contribution of  $d_{3z^2-r^2}$  and  $d_{x^2-y^2}$  are found in the charge density around Mn atoms. Eventually, all four Mn atoms are identical when the structure reaches the cubic symmetry in Struct 4. It can also be confirmed by the projected DOS, as shown in Fig. 4d, both  $d_{3z^2-r^2}$  and  $d_{x^2-y^2}$  orbital projected DOS distributions for Mn 1 and Mn 2 in Struct 3, tend to be similar near fermi level. The projected DOS also shows that orbital order completely vanishes in Struct 4 (Supplementary Fig. 11). Thus, we conclude that as the octahedral rotation and Jahn–Teller distortion are systematically suppressed the symmetry of the lattice structure is enhanced, which not only strengthens the ferromagnetic interaction but also closes the gaps (indirect and direct) near the Fermi level.

## DISCUSSION

Although the exact role of thermal heating in ultrafast pump-probe experiments remains controversial and not well understood, we calculate the temperature rise caused by the absorption of a single pulse using  $\Delta T = E^*/C$ <sup>45</sup>, where  $E^* = 50 \pm 30 \text{ J g}^{-1}$  (pump fluence of  $6 \text{ mJ cm}^{-2}$ ) is the energy absorbed per pulse<sup>46–48</sup>. Using the heat capacity  $C = 0.4135 \text{ J g}^{-1} \text{ K}^{-1}$  of LaMnO<sub>3</sub> at room temperature<sup>49</sup>,

**Table 1.** The rotation angles and Jahn–Teller distortion ( $Q_2$ ,  $Q_3$ ) for the four atomic structures in first-principles calculations. Definition of Jahn–Teller distortion amplitudes  $Q_2$  and  $Q_3$  is shown in Supplementary Fig. 11.

	Struct 1 ( $t = 0$ ps)	Struct 2	Struct 3	Struct 4
Rotation angle for two ‘-’ axes	7.5°	4.5°	2.0°	0
Rotation angle for the ‘+’ axis	6.0°	3.0°	2.0°	0
Jahn–Teller ( $Q_2$ ) (Å)	0.19	0.19	0.015	0
Jahn–Teller ( $Q_3$ ) (Å)	0.13	0.13	0.047	0

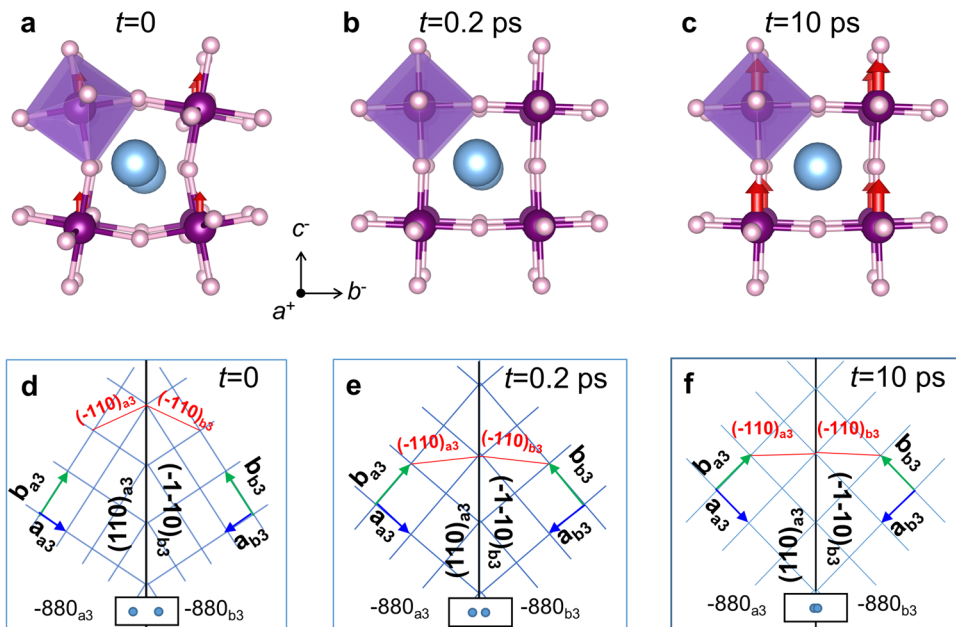


**Fig. 5 Evolution of the orthorhombicity and Jahn–Teller distortion in the  $\text{LaMnO}_3$  freestanding film.** **a–c** Schematic of the photoinduced structural change at (a)  $t = 0$ , (b)  $t = 0.2$  ps and (c)  $t = 10$  ps due to the change of  $\text{MnO}_6$  octahedral tilt and La displacement. The red arrows in the (a) and (b) represent the spin order. **d–f** Schematic of evolution of the orthorhombicity ( $a/b$  ratio) of a pair of twin variants ( $a^+b^-c^-_3$  and  $a^-b^+c^-_3$ ) at time delay (d)  $t = 0$ , (e)  $t = 0.2$  ps and (f)  $t = 10$  ps in the [001] projection. Note,  $a^+b^-c^-_3$  and  $a^-b^+c^-_3$  have the (110) reflection twinning relationship in which  $(110)_{a3} \parallel (-1-10)_{b3}$  (twin boundary is indicated by the black line). The subscripts a3 and b3 represent twin variant  $a^+b^-c^-_3$  and  $a^-b^+c^-_3$ , respectively. When  $a/b < 1$ ,  $(-110)_{a3}$  is not parallel to  $(-110)_{b3}$  (red lines), resulting in the spot splitting of  $-k\bar{k}0$  (bottom insets). When the  $a/b$  ratio moves toward the unity, spot splitting reduces and vanishes when  $a/b = 1$  [ $(-110)_{a3} \parallel (-110)_{b3}$ ]. Note, the drawing of the lattice is exaggerated for clarity. For the complete description of twelve equivalent twin variants in the system and their corresponding diffraction patterns, please see Supplementary Fig. 7.

temperature rise of  $120$  ( $\pm 80$ ) K can be estimated. The uncertainty comes from the fact that the relaxation channels of the absorbed photon energy are not clear<sup>50</sup>. However, using the thermal expansion coefficient  $(\Delta a/a_0)/(\Delta T) = 1.06 \times 10^{-5} \text{ K}^{-1}$  of  $\text{LaMnO}_3$ <sup>51,52</sup> and the experimental value of  $\Delta a/a_0 = 3.5 \times 10^{-4}$  (Supplementary Fig. 8c), the temperature rise is estimated to be about  $33$  K. More studies are needed to clarify the heating effect. It should be noted that from the measurements of the La peaks in the Fig. 3b, the intensity drop observed is about  $30\%$ , which corresponds to the reduction of  $16\%$  of La displacement using  $I \propto d^2$ <sup>36</sup>, where  $I$  is the diffraction intensity and  $d$  is the La displacement. Compared from the temperature dependence of La displacement through the structural transition of the orthorhombic  $\text{LaMnO}_3$ <sup>52</sup>, the  $16\%$  reduction corresponds to about  $350$  K temperature increase which is much larger than the estimated temperature rise in the current experiment. Furthermore, the Bragg peak intensity essentially remains constant except for the fast bump observed in the initial  $0.5$  ps, which indicates that atomic thermal vibration is negligible. Therefore, the observed ultrafast structural evolution with distinct

orthorhombicity change is very different from the thermal equilibrium phase transitions.

Through the UED experiments and simulations, we have captured snapshots of the atomic motion in  $\text{LaMnO}_3$  membranes upon photoexcitation with high temporal resolution. The observed lattice evolution with characteristic structural components is illustrated in Fig. 5a–c. Immediately after the laser excitation, light is absorbed between the  $e_g^1$  and  $e_g^2$  bandgap which is about  $1.6$  eV, close to the energy of the  $800$  nm photons. Then, during the first time period of  $0$ – $0.2$  ps, both the oxygen and La displacements including the existing Jahn–Teller distortion are significantly reduced. However, during the second time period of  $0.2$ – $10$  ps, some motions of oxygen atoms stop while the La atoms continue. Apparently the difference can be attributed to different time dependence of the in-phase rotation, the out-of-phase rotation, the Jahn–Teller distortion and the La cation displacement. In a deeper understanding, the different time dependence is related to the different optical phonon modes coupled to the oxygen and the La atoms. The former is usually associated with much faster phonons ( $> 7$  THz for the rotational mode and  $> 14$  THz

for the Jahn-Teller mode) than the latter ( $\sim 2.5$  THz)<sup>53</sup>, which could relax oxygen atoms to the quasi-equilibrium position faster than the La atoms. Since we did not detect similar trend in the Bragg peak intensities, we can exclude long-range order-disorder transition as a source for the diffraction dynamics. The La and oxygen peak intensity change can then be ascribed to the decreased atomic displacements due to the electron lattice interaction in a excited state with electron hole pairs<sup>39</sup>. On the other hand, the full orthorhombic lattice dynamics, initiating from  $t = 0$  and slowly ending at  $t = 10$  ps, are evidenced by the Bragg peak shape change and the La diffraction peak position change, both with an almost linear time dependence. The slow lattice change could be explained by the acoustic phonon mediated strain relaxation from the surface to the interior of the film<sup>54</sup> as well as the lateral constrain set by the orthorhombic domain, or twin boundaries. Two acoustic phonon modes of about 0.12 and 0.07 THz were indeed observed in Fourier transformations of both Bragg and La peak intensities from  $t = 0$  to  $t = 40$  ps in Supplementary Fig. 9b. The acoustic phonon frequency  $f = \frac{v}{2d}$  agrees well with the calculated pressure wave that results from the inhomogeneous strain across the film thickness<sup>55,56</sup>, where  $d$  is the thickness and  $v$  is the acoustic wave velocity. Using the known film thickness of  $\sim 20$  nm and the sound velocity of  $v_l = 4880$  m s $^{-1}$  (longitudinal polarization) and  $v_t = 2920$  m s $^{-1}$  (transverse polarization) at 300 K<sup>57</sup>, the calculated frequencies are indeed about 0.12 and 0.07 THz. Thus, it is expected that within about one period of the acoustic phonon, the original orthorhombic lattice fully relaxes to the metastable state with significantly reduced orthorhombicity, i.e. reduced atomic displacements, with increased lattice symmetry toward domain coalescence. As shown in Fig. 5d-f the  $a^+b^-c^-$  and  $a^-b^+c^-$  domains coalesce together as a result of the reduction in lattice orthorhombicity, which increases the average domain size and decreases the width of the diffraction peaks.

Our first principles calculations imply that the ferromagnetism may be enhanced following the changes in lattice structure. In thin films of LaMnO<sub>3</sub>, ferromagnetic insulating state is the mostly observed ground state due to the epitaxial lattice structure, which persists in the current freestanding films (see Supplementary Fig. 2). It is known that in La-doped CMR manganite oxides, the octahedral rotation is weaker than other manganite oxides since La is the largest rare-earth element and the tolerance factor of the ABO<sub>3</sub> structure is closer to 1 when A is La. It is also known that a more symmetric structure with less octahedral rotation and Jahn-Teller distortion favors the ferromagnetic superexchange or double-exchange interaction over the antiferromagnetic superexchange interaction. Thus, in the current study, it is reasonable to consider a transient state with enhanced ferromagnetism in LaMnO<sub>3</sub>. Meanwhile the straightened Mn-O-Mn bond increases the bandwidth of Mn e<sub>g</sub> orbitals, as shown in Supplementary Fig. 11, yielding enhanced conductivity. Such a strong ferromagnetic and metallic state in the light-excited state is different from a comparable magnetic and conducting phase in thermal equilibrium in two aspects. One is that in equilibrium, the phase change is usually achieved either by carrier doping or lowering the temperature. Both are not employed in the current study. The temperature of the film is slightly enhanced by about 35 K, instead of being decreased. Since the ferromagnetic interaction energy is increased as shown in the DFT calculations, it is possible to maintain the ferromagnetic state at temperatures much higher than the Curie temperature of 125 K (see Supplementary Fig. 2) in the thermal equilibrium phase. Our prediction of photoinduced ferromagnetism in LaMnO<sub>3</sub> might inspire future experimental verification.

In summary, we report the study of the structural dynamics of a freestanding LaMnO<sub>3</sub> film with a state-of-the-art MeV UED instrument. We find the key structural ingredients including lattice orthorhombicity and Jahn-Teller distortion related atomic

displacements (oxygen off-centering, La off-centering) and octahedral rotation are suppressed upon photoexcitation in a thermally non-achievable process with different time scales. At the time of 10 ps after the excitation, the material system enters a quasi-equilibrium state in which we find enhanced ferromagnetic order and an insulator to metal transition using first principles calculations. Our study has opened up possibilities to manipulate strongly correlated interactions among charge, orbital, spin, and lattice and harness emergent functionalities in freestanding oxides, particularly those not achievable in thermal equilibrium at ambient conditions.

## METHODS

### Sample fabrication

The (0 0 1) SrTiO<sub>3</sub> substrates with atomically flat TiO<sub>2</sub> surface termination were obtained after a buffered hydrofluoric (HF) acid etching and an oxygen annealing at 950 °C for 1 h. The Sr<sub>3</sub>Al<sub>2</sub>O<sub>6</sub> layer was grown first on the top of the SrTiO<sub>3</sub> substrate followed by the growth of LaMnO<sub>3</sub> layer using stoichiometric Sr<sub>3</sub>Al<sub>2</sub>O<sub>6</sub> and LaMnO<sub>3</sub> targets in a reflective high-energy electron diffraction (RHEED) assisted pulsed laser deposition (PLD) system. The Sr<sub>3</sub>Al<sub>2</sub>O<sub>6</sub> layer was grown at a substrate temperature of 860 °C with an oxygen pressure of  $1 \times 10^{-4}$  mbar. For the PLD deposition, a 248 nm KrF excimer laser with an applied energy density of 1.02 J cm $^{-2}$  was used. The LaMnO<sub>3</sub> layer was grown with a substrate temperature of 780 °C, an oxygen pressure of  $1 \times 10^{-2}$  mbar and a laser energy density of 2 J cm $^{-2}$ . The thickness of the layer was 50 unit cells (20 nm) which was monitored by RHEED intensity oscillations.

To obtain freestanding films, poly (methyl methacrylate) (PMMA) was spin-coated on top of the LaMnO<sub>3</sub> surface and heated at 150 °C for 10 min. Then the coated sample was immersed in deionized water at room temperature until the Sr<sub>3</sub>Al<sub>2</sub>O<sub>6</sub> buffer layer was completely dissolved, which yielded the PMMA-supported LaMnO<sub>3</sub> film. Furthermore, the hollow copper grid was used to pick up the floating LaMnO<sub>3</sub>/PMMA sample, which was then annealed at 100 °C for 5 min to remove the water. Finally, the chloroform solution was used to dissolve the top PMMA layer and obtain the freestanding film.

### MeV ultrafast electron diffraction (MeV-UED) experiments

The MeV-UED experiments were conducted using the recently developed electron beam compression scheme with a double bend achromat compressor<sup>28</sup> in Shanghai Jiaotong University. The electron beam with a kinetic energy of 3 MeV was generated in a photocathode radio-frequency gun and further compressed to reduce both the pulse width and timing jitter. For exciting the freestanding film, a pump laser pulse with 800 nm wavelength (1.55 eV) and  $\sim 30$  fs (FWHM) pulse duration operating at 100 Hz was used. The spot size of the pump light is 1.5 mm, which is about five times larger than the electron beam and ensures homogenous excitation. The excitation energy fluence of the femtosecond laser was kept at 6 mJ cm $^{-2}$  for all the UED measurements. The diffraction pattern is captured by a phosphor screen imaged onto an electron-multiplying charge-coupled device camera. The time delay between the pump laser and the electron beam is adjusted by a translational stage and the final diffraction patterns are averaged over multiple scans to attain a high signal-to-noise ratio. The error range of the intensity is 0.16–0.88%, and 0.34–0.42% for the  $\Delta$ FWHM, and 0.009–0.012% for  $\Delta\mathbf{Q}$ .

### UED simulations

Dynamical electron diffraction patterns were calculated based on Bloch wave method using the computer codes developed in-house at Brookhaven National Laboratory. To take crystal symmetry and 12 equivalent crystal variants in the system into account we first calculated diffraction pattern from individual twin variant, and then average all of them into a single diffraction pattern. The averaged pattern is further convoluted with a point spread function  $\text{FWHM} = 0.043$  Å $^{-1}$  to account for beam broadening effect from the UED instrument.

### First-principles calculations

The electronic and magnetic properties of LaMnO<sub>3</sub> films were elucidated using first-principles DFT calculations, as implemented in Vienna Ab initio

Simulation Package (VASP)<sup>58,59</sup>. The ion–electron interactions were described by the projector-augmented wave method. We used the generalized gradient approximation (GGA) with Perdew–Burke–Erzenhof solids-adapted exchange correlation functional (PBEsol)<sup>60,61</sup>. Static local electronic correlations were added to the GGA exchange-correlation potential in the GGA +  $U$  method with  $U = 3.5$  eV and  $J = 0.9$  eV (Mn<sub>3d</sub>) as C. Zhong et al.<sup>44</sup>. In our calculations, the atomic positions of structure in Fig. 4a are relaxed until the force on each atom is  $<0.01$  eV Å<sup>-1</sup>, and all of the self-consistent electronic calculations are converged to 10<sup>-6</sup> eV per cell, and a  $4 \times 5 \times 5$   $\mathbf{k}$ -point mesh is employed for the LaMnO<sub>3</sub> unit cells, and 30  $\mathbf{k}$ -points were sampled along each of the high symmetry lines in the Brillouin zone to obtain the band structures.  $\sqrt{2} \times \sqrt{2} \times 2$  supercells with lattice constant same as those from experiments were used in the calculations.

## DATA AVAILABILITY

All data needed to evaluate the conclusions in the paper are present in the paper and/or the Supplementary Materials.

Received: 25 August 2021; Accepted: 23 March 2022;

Published online: 20 April 2022

## REFERENCES

1. Basov, D. N. et al. Electrodynamics of correlated electron materials. *Rev. Mod. Phys.* **83**, 471–541 (2011).
2. Basov, D. N., Averitt, R. D. & Hsieh, D. Towards properties on demand in quantum materials. *Nat. Mater.* **16**, 1077–1088 (2017).
3. Buzzi, M., Först, M., Mankowsky, R. & Cavalleri, A. Probing dynamics in quantum materials with femtosecond X-rays. *Nat. Rev. Mater.* **3**, 299–311 (2018).
4. Sun, Z. & Millis, A. J. Transient trapping into metastable states in systems with competing orders. *Phys. Rev. X* **10**, 021028 (2020).
5. Kogar, A. et al. Light-induced charge density wave in LaTe<sub>3</sub>. *Nat. Phys.* **16**, 159–163 (2020).
6. Zhou, F. et al. Nonequilibrium dynamics of spontaneous symmetry breaking into a hidden state of charge-density wave. *Nat. Commun.* **12**, 566 (2021).
7. Fausti, D. et al. Light-induced superconductivity in a stripe-ordered cuprate. *Science* **331**, 189–191 (2011).
8. Hu, W. et al. Optically enhanced coherent transport in YBa<sub>2</sub>Cu<sub>3</sub>O<sub>6.5</sub> by ultrafast redistribution of interlayer coupling. *Nat. Mater.* **13**, 705–711 (2014).
9. Mankowsky, R. et al. Nonlinear lattice dynamics as a basis for enhanced superconductivity in YBa<sub>2</sub>Cu<sub>3</sub>O<sub>6.5</sub>. *Nature* **516**, 71–73 (2014).
10. Mitrano, M. et al. Possible light-induced superconductivity in K<sub>3</sub>C<sub>60</sub> at high temperature. *Nature* **530**, 461–464 (2016).
11. Ichikawa, H. et al. Transient photoinduced ‘hidden’ phase in a manganite. *Nat. Mater.* **10**, 101–105 (2011).
12. Rini, M. et al. Control of the electronic phase of a manganite by mode-selective vibrational excitation. *Nature* **449**, 72–74 (2007).
13. Först, M. et al. Nonlinear phononics as an ultrafast route to lattice control. *Nat. Phys.* **7**, 854–856 (2011).
14. Yang, Z., Ko, C. & Ramanathan, S. Oxide electronics utilizing ultrafast metal–insulator transitions. *Annu. Rev. Mater. Res.* **41**, 337–367 (2011).
15. Ichikawa, H. et al. Transient photoinduced ‘hidden’ phase in a manganite. *Nat. Mater.* **10**, 101–105 (2011).
16. Li, T. et al. Femtosecond switching of magnetism via strongly correlated spin-charge quantum excitations. *Nature* **496**, 69–73 (2013).
17. Beaud, P. et al. A time-dependent order parameter for ultrafast photoinduced phase transitions. *Nat. Mater.* **13**, 923–927 (2014).
18. Nova, T. F., Disa, A. S., Fechner, M. & Cavalleri, A. Metastable ferroelectricity in optically strained SrTiO<sub>3</sub>. *Science* **364**, 1075–1079 (2019).
19. Li, X. et al. Terahertz field-induced ferroelectricity in quantum paraelectric SrTiO<sub>3</sub>. *Science* **364**, 1079–1082 (2019).
20. Li, Q. et al. Subterahertz collective dynamics of polar vortices. *Nature* **592**, 376–380 (2021).
21. Eichberger, M. et al. Snapshots of cooperative atomic motions in the optical suppression of charge density waves. *Nature* **468**, 799–802 (2010).
22. Baum, P., Yang, D.-S. & Zewail, A. H. 4D visualization of transitional structures in phase transformations by electron diffraction. *Science* **318**, 788–792 (2007).
23. Morrison, V. R. et al. A photoinduced metal-like phase of monoclinic VO<sub>2</sub> revealed by ultrafast electron diffraction. *Science* **346**, 445–448 (2014).
24. Zong, A. et al. Evidence for topological defects in a photoinduced phase transition. *Nat. Phys.* **15**, 27–31 (2018).
25. Konstantinova, T. et al. Nonequilibrium electron and lattice dynamics of strongly correlated Bi<sub>2</sub>Sr<sub>2</sub>CaCu<sub>3</sub>O<sub>8+δ</sub> single crystals. *Sci. Adv.* **4**, eaap7427 (2018).
26. Li, J. et al. Dichotomy in ultrafast atomic dynamics as direct evidence of polaron formation in manganites. *npj Quantum Mater.* **1**, 16026 (2016).
27. Duan, S. et al. Optical manipulation of electronic dimensionality in a quantum material. *Nature* **595**, 239–244 (2021).
28. Qi, F. et al. Breaking 50 femtosecond resolution barrier in MeV ultrafast electron diffraction with a double bend achromat compressor. *Phys. Rev. Lett.* **124**, 134803 (2020).
29. Sie, E. J. et al. An ultrafast symmetry switch in a Weyl semimetal. *Nature* **565**, 61–66 (2019).
30. Lu, D. et al. Synthesis of freestanding single-crystal perovskite films and heterostructures by etching of sacrificial water-soluble layers. *Nat. Mater.* **15**, 1255–1260 (2016).
31. Ji, D. et al. Freestanding crystalline oxide perovskites down to the monolayer limit. *Nature* **570**, 87–90 (2019).
32. Dong, G. et al. Super-elastic ferroelectric single-crystal membrane with continuous electric dipole rotation. *Science* **366**, 475–479 (2019).
33. Hong, S. S. et al. Extreme tensile strain states in La<sub>0.7</sub>Ca<sub>0.3</sub>MnO<sub>3</sub> membranes. *Science* **368**, 71–76 (2020).
34. Zhai, X. et al. Correlating interfacial octahedral rotations with magnetism in (LaMnO<sub>3+δ</sub>)<sub>n</sub>/(SrTiO<sub>3</sub>)<sub>n</sub> superlattices. *Nat. Commun.* **5**, 5283 (2014).
35. Glazer, A. M. The classification of tilted octahedra in perovskites. *Acta Crystallogr. B* **28**, 3384 (1972).
36. Brahlek, M. et al. Structural refinement of *Pbnm*-type perovskite films from analysis of half-order diffraction peaks. *J. Appl. Phys.* **121**, 045303 (2017).
37. Dong, Y. et al. Interfacial octahedral manipulation imparts hysteresis-free metal to insulator transition in ultrathin nickelate heterostructure. *Adv. Mater. Interfaces* **6**, 1900644 (2019).
38. Wu, L. & Zhu, Y. Transformation twinning in carbon-doped PrCo<sub>2</sub> magnetic crystals. *Philos. Mag. A* **76**, 481–492 (1997).
39. Porer, M. et al. Ultrafast relaxation dynamics of the antiferrodistortive phase in Ca doped SrTiO<sub>3</sub>. *Phys. Rev. Lett.* **121**, 055701 (2018).
40. Amelitchev, V. A. et al. Structural and chemical analysis of colossal magnetoresistance manganites by Raman spectrometry. *Phys. Rev. B* **63**, 104430 (2001).
41. Beaud, P. et al. Ultrafast structural phase transition driven by photoinduced melting of charge and orbital order. *Phys. Rev. Lett.* **103**, 155702 (2009).
42. Caviezel, A. et al. Femtosecond dynamics of the structural transition in mixed valence manganites. *Phys. Rev. B* **86**, 174105 (2012).
43. Dagotto, E., Hotta, T. & Moreo, A. Colossal magnetoresistant materials: the key role of phase separation. *Phys. Rep.* **344**, 1–135 (2001).
44. Zhong, C. et al. Strain-induced insulating ferromagnetism in LaMnO<sub>3</sub> thin films from first-principles investigations. *J. Magn. Magn.* **466**, 406 (2018).
45. Wen, H. et al. Electronic origin of ultrafast photoinduced strain in BiFeO<sub>3</sub>. *Phys. Rev. Lett.* **110**, 037601 (2013).
46. Arima, T., Tokura, Y. & Torrance, J. B. Variation of optical gaps in perovskite-type 3d transition-metal oxides. *Phys. Rev. B* **48**, 17006 (1993).
47. Jung, J. H. et al. Determination of electronic band structures of CaMnO<sub>3</sub> and LaMnO<sub>3</sub> using optical-conductivity analyses. *Phys. Rev. B* **55**, 15489 (1997).
48. Kim, M. W. et al. Origin of the 2 eV peak in optical absorption spectra of LaMnO<sub>3</sub>: an explanation based on the orbitally degenerate Hubbard model. *N. J. Phys.* **6**, 156–156 (2004).
49. Woodfield, B. F., Wilson, M. L. & Byers, J. M. Low-temperature specific heat of La<sub>1-x</sub>Sr<sub>x</sub>MnO<sub>3-6</sub>. *Phys. Rev. Lett.* **78**, 3201 (1997).
50. Huang, L., Callan, J. P., Glezer, E. N. & Mazur, E. GaAs under intense ultrafast excitation: response of the dielectric function. *Phys. Rev. Lett.* **80**, 185 (1998).
51. Miyoshi, S. et al. In situ XRD study on oxygen-excess LaMnO<sub>3</sub>. *Solid State Ion.* **175**, 383–386 (2004).
52. Thygesen, P. M. M. et al. Local structure study of the orbital order/disorder transition in LaMnO<sub>3</sub>. *Phys. Rev. B* **95**, 174107 (2017).
53. Iliev, M. et al. Raman spectroscopy of orthorhombic perovskitelike Ymno<sub>3</sub> and LaMnO<sub>3</sub>. *Phys. Rev. B* **57**, 2872 (1998).
54. Chin, A. H. et al. Ultrafast structural dynamics in InSb probed by time-resolved X-ray diffraction. *Phys. Rev. Lett.* **83**, 336 (1999).
55. Karam, T. E., Hu, J. & Blake, G. A. Strongly coupled electron–phonon dynamics in few-layer TiSe<sub>2</sub> exfoliates. *ACS Photonics* **5**, 1228–1234 (2018).
56. Harb, M. et al. Excitation of longitudinal and transverse coherent acoustic phonons in nanometer free-standing films of (001) Si. *Phys. Rev. B* **79**, 094301 (2009).
57. Ewe, L. S. & Abd-Shukor, R. Elastic moduli and sound velocity in La<sub>1-x</sub>Sr<sub>x</sub>MnO<sub>3</sub> (x = 0 to 0.3). *Int. J. Mod. Phys. B* **24**, 465–478 (2012).
58. Kresse, G. & Furthmüller, J. Efficiency of ab-initio total energy calculations for metals and semiconductors using a plane-wave basis set. *Comput. Mater. Sci.* **6**, 15–50 (1996).
59. Kresse, G. & Furthmüller, J. Self-interaction correction to density-functional approximations for many-electron systems. *Phys. Rev. B* **54**, 11169 (1996).

60. Perdew, J. et al. Restoring the density-gradient expansion for exchange in solids and surfaces. *Phys. Rev. Lett.* **100**, 136406 (2008).
61. Perdew, J., Burke, K. & Ernzerhof, M. Generalized gradient approximation made simple. *Phys. Rev. Lett.* **77**, 3865 (1996).

## ACKNOWLEDGEMENTS

We acknowledge support from the National Key R&D Program of China (No. 2021YFA1400202), the Science and Technology Commission of Shanghai Municipality (Nos. 21JC1405000 and 16DZ2260200), the National Science Foundation of China (Grant Nos. 52072244, 11925505, 11504232 and 11721091), ShanghaiTech Startup Fund. The work at Brookhaven was supported by US DOE, Basic Energy Sciences, Materials Sciences and Engineering Division under Contract No. DE-SC0012704.

## AUTHOR CONTRIBUTIONS

D.X. and X.Z. conceived the project. Y.Z. supervised the data interpretation and diffraction simulation. J.Z. supervised the first principles calculation. Q.L. fabricated the samples. Y.C. performed the MeV-UED experiments. L.W. and Y.Z. performed the twinning analysis and UED simulations. H.G. performed the first principles calculation. Q.L., Y.C. and L.W. analyzed the experimental data. Q.L., Y.C., H.G., L.W., D.X., X.Z. wrote the manuscript and Y.Z. revised the manuscript. All the authors discussed the results and contributed to the manuscript preparation.

## COMPETING INTERESTS

The authors declare no competing interests.

## ADDITIONAL INFORMATION

**Supplementary information** The online version contains supplementary material available at <https://doi.org/10.1038/s41535-022-00456-4>.

**Correspondence** and requests for materials should be addressed to Dao Xiang, Jin Zhao, Yimei Zhu or Xiaofang Zhai.

**Reprints and permission information** is available at <http://www.nature.com/reprints>

**Publisher's note** Springer Nature remains neutral with regard to jurisdictional claims in published maps and institutional affiliations.



**Open Access** This article is licensed under a Creative Commons Attribution 4.0 International License, which permits use, sharing, adaptation, distribution and reproduction in any medium or format, as long as you give appropriate credit to the original author(s) and the source, provide a link to the Creative Commons license, and indicate if changes were made. The images or other third party material in this article are included in the article's Creative Commons license, unless indicated otherwise in a credit line to the material. If material is not included in the article's Creative Commons license and your intended use is not permitted by statutory regulation or exceeds the permitted use, you will need to obtain permission directly from the copyright holder. To view a copy of this license, visit <http://creativecommons.org/licenses/by/4.0/>.

© The Author(s) 2022